Structure
Article

The Crystal Structures of the Eukaryotic Chaperonin CCT Reveal Its Functional Partitioning

Nir Kalisman,[1] Gunnar F. Schröder,[2,3,*] and Michael Levitt[1,*]
[1]Department of Structural Biology, Stanford University School of Medicine, Stanford, CA 94305, USA
[2]Institute of Complex Systems (ICS-6), Forschungszentrum Jülich, 52425 Jülich, Germany
[3]Physics Department, Heinrich-Heine University, 40225 Düsseldorf, Germany
*Correspondence: gu.schroeder@fz-juelich.de (G.F.S.), michael.levitt@stanford.edu (M.L.)
http://dx.doi.org/10.1016/j.str.2013.01.017

SUMMARY

In eukaryotes, CCT is essential for the correct and efficient folding of many cytosolic proteins, most notably actin and tubulin. Structural studies of CCT have been hindered by the failure of standard crystallographic analysis to resolve its eight different subunit types at low resolutions. Here, we exhaustively assess the R value fit of all possible CCT models to available crystallographic data of the closed and open forms with resolutions of 3.8 Å and 5.5 Å, respectively. This unbiased analysis finds the native subunit arrangements with overwhelming significance. The resulting structures provide independent crystallographic proof of the subunit arrangement of CCT and map major asymmetrical features of the particle onto specific subunits. The actin and tubulin substrates both bind around subunit CCT6, which shows other structural anomalies. CCT is thus clearly partitioned, both functionally and evolutionary, into a substrate-binding side that is opposite to the ATP-hydrolyzing side.

INTRODUCTION

Group II chaperonins are large nanomachines that are central to protein folding in both eukaryotes and archaea. The overall structure is 16 nm in diameter and comprises two stacked rings of eight subunits each (Yébenes et al., 2011). Through a cycle that is powered by ATP hydrolysis, these subunits rotate to open and close a central folding chamber. While the archaeal systems are often homo-oligomeric (Kapatai et al., 2006), the eukaryotic chaperonin has evolved (Archibald et al., 2001) to a hetero-oligomeric complex, where each ring is made of eight paralogous subunits (CCT1 to CCT8) with a mutual sequence identity of about 30%. This divergence to eight genes occurred very early in eukaryotic evolution and is highly conserved in all eukaryotic species. The hetero-oligomeric nature of CCT plays a key role in CCT function by allowing for intricate substrate-binding modes in the open form (Llorca et al., 2001; Spiess et al., 2006) and differential ATP hydrolysis in the closed form (Rivenzon-Segal et al., 2005; Amit et al., 2010). This functionality is tightly coupled to a precise arrangement of the eight subunits within each ring and to a fixed relative registration of the two rings (Martín-Benito et al., 2007).

Much of the structural knowledge on group II chaperonins comes from high-resolution crystallography of archaeal systems (Ditzel et al., 1998; Shomura et al., 2004). In contrast, structural studies of CCT either by crystallography (Dekker et al., 2011; Muñoz et al., 2011) or by cryo-electron microscopy (EM) (Martín-Benito et al., 2007; Cong et al., 2010) could not achieve the sufficient resolution to unambiguously identify the different subunits within the electron density. Specifically, the high sequence similarity between the subunits dictates a highly similar backbone trace for all subunits. This limitation can only be overcome by resolving subunit-specific side-chains. Unfortunately, none of these studies had side-chain densities of sufficient quality to make such direct inference. As a consequence, questions pertaining to the hetero-oligomeric nature of CCT have remained unresolved, the most basic of which was that of the subunit arrangement in the native complex. This question is difficult to answer, as there are eight factorial (8! = 40,320) possible arrangements of the subunits within a particle.

To resolve the subunit ambiguity, we present a different approach to low-resolution crystallography, where we abandon the conventional search for specific side-chain densities with the aid of a crystallographic browser. Instead, we collectively and automatically assess the fit of many side-chains of a specific model to the crystallographic data. This automation allows us to test millions of models and to determine objectively if one of them fits the data better than others. When applied to the two crystallographic data sets of CCT that have been published to date, this approach successfully singles out with very high confidence one model for each set. These models describe how to locate the different subunits within the crystal asymmetric units and allow us to fully solve the CCT structures. The resulting structures not only give crystallographic proof of the native subunit arrangement of CCT but also map various asymmetric features to specific subunits. We find that subunit CCT6-Z shows significant structural deviations from the other subunits. We also find that actin and tubulin, the main substrates of CCT, bind mainly around this subunit. The overall picture that emerges is that of a partitioned particle, where specific functions, such as substrate binding or ATP hydrolysis, cluster to specific sides.

RESULTS

Identifying Subunits in the Crystal Asymmetric Units

In this study, we reanalyze X-ray diffraction data of the closed form of yeast-CCT at 3.8 Å resolution (Dekker et al., 2011) and the open form of bovine-CCT at 5.5 Å resolution (Muñoz et al., 2011). Our first aim was to assign the correct subunit type to each position in the two crystal asymmetric units. This problem is harder than determining the subunit arrangement of the particle alone, because each arrangement can fit into the electron density in eight different orientations (Figures 1A and 1D). There are, therefore, 2,580,480 (= 8! × 8 × 8) and 322,560 (= 8! × 8) possible models for the asymmetric units of the closed and open data sets, respectively. Because of the large number of possible models and the low resolution of the data, we strictly adhered to an unbiased approach that did not use calculated phases. Thus, we exhaustively built all the possible all-atom models for both asymmetric units and then measured their fit to the crystallographic data by calculating their R values (Vaguine et al., 1999) without doing any refinement. While our fit measure is straightforward, much consideration went into the model building step. First, all our models for a particular form had exactly the same backbone without regard for the specific subunit arrangement or orientation; models differed only in the side-chain atoms added to this fixed backbone. Second, the side-chain rotamers were modeled by SCWRL4 (Krivov et al., 2009) on a backbone taken from an archaeal chaperonin (Shomura et al., 2004).

Without any prior information, the histogram of R values obtained for the closed form (Figure 1B) singles out one model of the asymmetric unit as having the best fit to the data (R_{cryst} = 49.7%; Z-score = −10.1). This model leads by a large margin over the nearly identical second-best model (R_{cryst} = 49.86%; Z-score = −8.0), in which the order of two subunits in the ring is swapped. In fact, the entire left tail of the distribution corresponds to models that are very similar to one another (Figure 1C) and gives the best R model as a consensus sequence. Independent support for this model comes from observing that its subunit arrangement is identical to that determined recently by studies that used cross-linking and mass spectrometry (Kalisman et al., 2012; Leitner et al., 2012; Herzog et al., 2012). For comparison, we also mark in Figure 1B the R values of two other subunit arrangements that were previously reported. The PW model (Dekker et al., 2011) was reported for the crystallographic data used here, and the LFC arrangement (Cong et al., 2010) was reported based on a cryo-EM reconstruction. These arrangements have a worse fit to the data with Z-scores of −1.6 and −0.8 for PW and LFC, respectively. Interestingly, we find that our model of the asymmetric unit reveals a perfect noncrystallographic dyad axis (perpendicular to the plane of Figure 1A) that relates the two particles.

The data set of the open form is much more challenging, not only because of the lower resolution (5.5 Å), but also because a third of the residues in one of the rings were previously reported as unstructured (Muñoz et al., 2011). Indeed, the R value histogram (Figure 1E) is not as clear-cut as for the closed form, and there is no one model that is decisively best. We note, however, that the subunit consensus (Figure 1F) of the top R value models gives a particle order of BDAGZEHA-BDAGZEHA, which is identical in 12 out of the 16 subunits to the arrangement found in the closed form or by cross-linking (BDAGZQHE-BDAGZQHE). This leaves no doubt as to how to orient the previously determined subunit arrangement in the asymmetric unit. In fact, we find the corresponding model to rank among the very top models in the histogram (R_{cryst} = 46.0%; rank #48). Observing so much side-chain signal in this very difficult crystallographic scenario is a remarkable finding. The resulting model of the asymmetric unit assigns the full subunit in the less structured ring as CCT6-Z and the protruding subunit in the more structured ring as CCT1-A. We note that this CCT6-Z subunit causes some steric interference in an adjacent molecule in the crystal and could be the reason for the protruding CCT1-A subunit in the latter.

Model Refinement

With the subunit arrangement and orientations in the asymmetric units well confirmed, we fully refined the initial models in both forms to reveal the atomic detail needed to explain CCT function. Application of the deformable elastic network (DEN) refinement (Brunger, 2007; Schröder et al., 2010) led to models with R_{free} of 41.5% and 39.8% for the closed and open forms, respectively. At this point, we continued to refine only the closed-form structure. Further iterations of manual model building and DEN refinement led to a final structure with R_{free} value of 28.37%. Complete refinement statistics for the closed and open form structures are reported in Table 1. CCT subunits contain several insertions of five to ten residues that are subunit-specific. These insertions coincided with additional electron densities (Figure 2A; Figure S2 available online) when they were structured or as clear breaks in the electron density when they were unstructured. We emphasize that these consistencies are independent support for the correctness of our subunit assignment and were not used in the assignment process itself.

Our closed-form structure compares favorably to two other structures that were previously reported for the same data set (Figure 2B). The structure of Dekker et al. (2011) accompanied their initial release of the crystallographic data and was based on an incorrect subunit arrangement (PW). It is therefore not surprising that its R_{free} value is six percentage points higher than ours and that its fit to the density is inferior (Figure 2C). Application of DEN refinement to this structure decreased its R_{free} value but not substantially. More recently, Leitner et al. reported a structure that was based on the correct subunit arrangement (OMS) and has R_{free} value that is two percentage points higher than ours. This difference in R_{free} value is likely not caused by the different core backbones, which superimpose to 0.9 Å root-mean-square deviation (rmsd). Rather, the structures differ considerably in the trace of the chain termini and internal loops and in the rotamers of some side-chains. We note that Leitner et al. (2012) based their structure on a particle arrangement that was derived from cross-linking data and did not systematically explore the fit of other possible arrangements or orientations to the data. We also note that their interpretation for the open form data set is wrong, incorrectly identifying the one protruding subunit as CCT7-H instead of CCT1-A.

The Weak CCT6-Z/CCT8-Q Interface

The interfaces between the eight subunits in the ring are significantly different, in spite of their high sequence similarity. In the

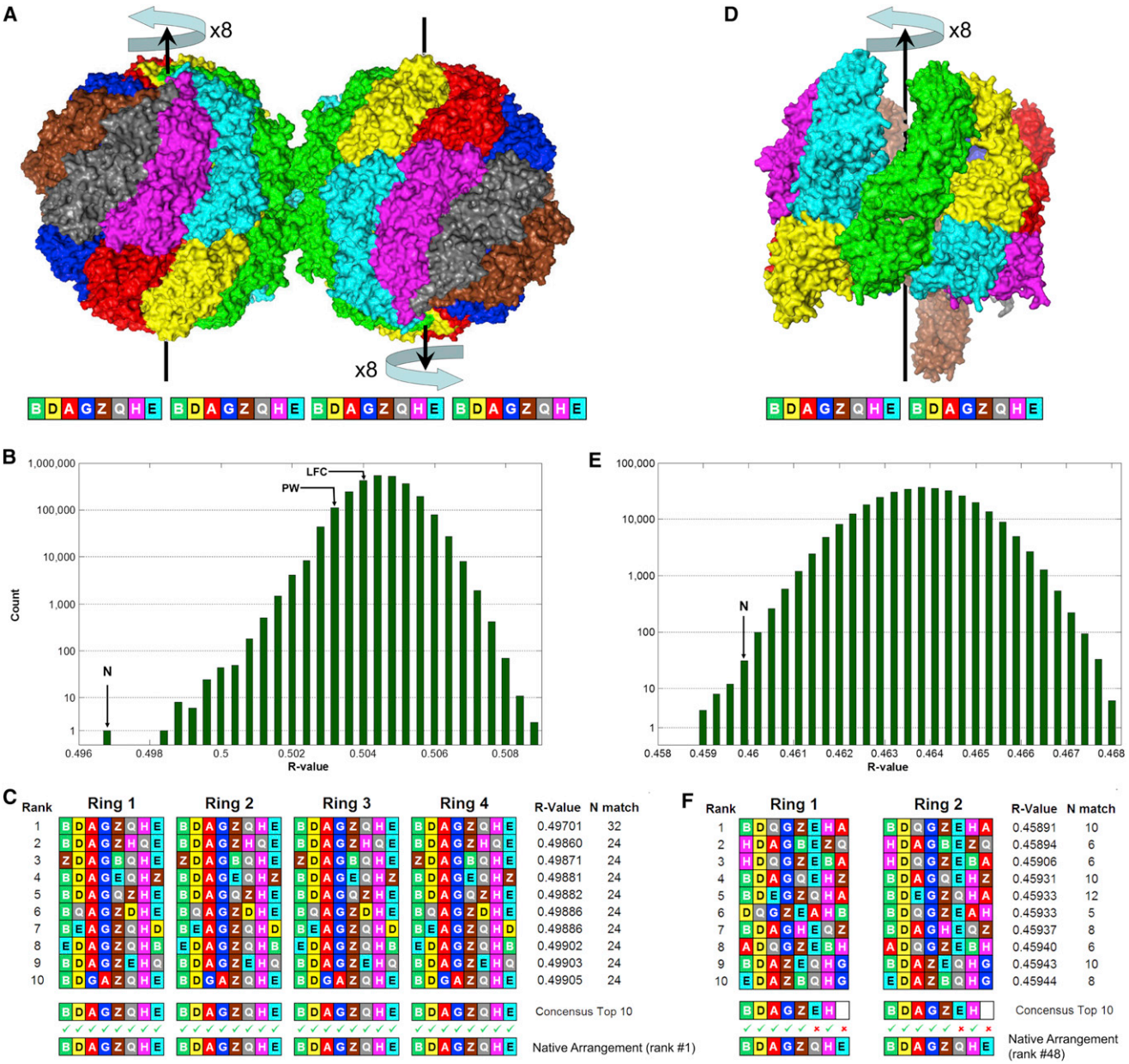

Figure 1. Identifying Subunits in the Crystal Asymmetric Units

(A) The asymmetric unit of the closed form contains two CCT particles, each with two rings of eight subunits, colored by subunit type; they are related by a perfect noncrystallographic dyad. There are 2,580,480 (= 8! × 8 × 8) possible models of the entire asymmetric unit. Each model can be described by a 32-letter string, where each letter denotes the subunit type in a certain position. Latin letters (A, B, G, D, E, Z, H, and Q) stand for subunits CCT1 to CCT8.

(B) The R value (calculated by SFCHECK; Vaguine et al., 1999) histogram for all 2,580,480 models reveals one model (N) to best fit the crystallographic data. Previously reported subunit arrangements, PW (Dekker et al., 2011) and LFC (Cong et al., 2010), are not distinguished.

(C) A consensus string of the ten left-most models from the histogram is identical to the model with the best R value.

(D) The crystal asymmetric unit of the open form contains one CCT particle with 322,560 (= 8! × 8) possible models.

(E) The R value histogram in this case is not as clear cut due to the lower resolution. The model (N) with the same subunit arrangement as for the closed form has a low R value.

(F) The consensus of the ten left-most models from the histogram is identical to the closed form consensus in 12 out of the 16 positions.

For more information about the insensitivity of the results to the method of R value calculation, whether the structure was refined, and the subset of side-chain atoms used, see Figure S1. That figure also shows that the SFCHECK R values for the closed form have a standard deviation of just 0.0001 or 0.01%.

closed form, the 6-Z/8-Q interface stands out as a particularly weak interface (Table 2; Figure 3A), with a total buried surface area that is only 63% of the average for a ring interface (2,595 Å^2). Moreover, this weakness is apparent throughout the entire interface and is not limited to specific domains of the subunits. Interestingly, the second-weakest interface (8-Q/7-H)

Table 1. Crystallographic Data and Refinement Statistics

Crystallographic Data	Closed Form	Open Form
reference	Dekker et al., 2011	Muñoz et al., 2011
space group	P1	$P2_12_12$
unit cell parameters	a = 159.10 Å	a = 272.7 Å
	b = 162.54 Å	b = 313.5 Å
	c = 268.10 Å	c = 158.3 Å
	α = 85.23°	
	β = 81.15°	
	γ = 61.17	
wavelength (Å)	1.00	1.114
resolution range (Å)	90.0–3.8	100.0–5.5
completeness (%)	91.6 (93.2)[a]	92.5 (95.3)[a]
mean $I/\sigma(I)$	8.4 (1.92)[a]	9.54 (1.2)[a]
highest resolution shell (Å)	4.0–3.8	6.0–5.5
Refinement		
resolution range (Å)	90.0–3.8	100.0–5.5
no. of reflections	209,671/10,483	44,462/2,238
(total/for R_{free})		
R_{work}/R_{free}	0.2479/0.2837	0.340/0.398
average isotropic	131.4	277.3
B-factor (Å^2)		
Number of Residues		
protein	32 chains[b]	16 chains
	16,716 structured residues	6,842 structured residues
	(95.5% of all residues)	(78.8% of all residues)
ADP	32[b]	
BeF_3	32[b]	
Mg^{2+}	32[b]	
rmsd		
bond angle rmsd (°)	1.62	0.65
bond length rmsd (Å)	0.0128	0.002
Ramachandran Statistics (%)		
favored	80.3	87.1
allowed	15.5	10.7
outliers	4.2	2.1

[a]In the highest resolution shell.
[b]NCS constraints enforced between the four octameric rings in the asymmetric units.

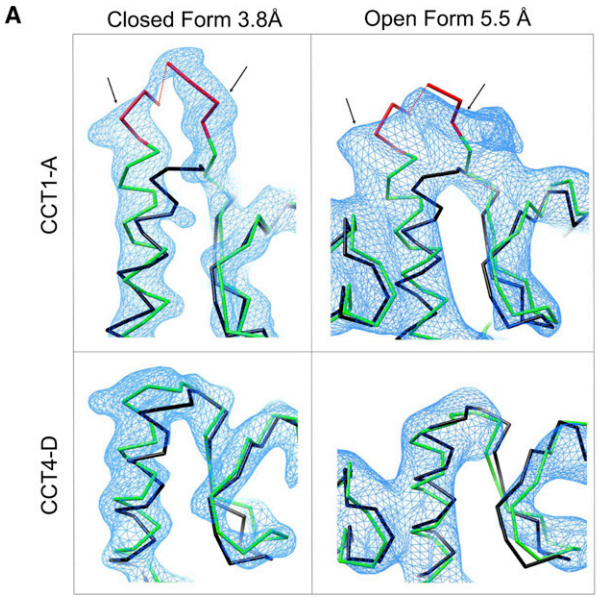

B

Coordinates	Arrang-ement	R_{work}	R_{free}	% All Residues
Closed Form (Yeast)				
Dekker et al. 2011	PW	30.7	34.4	95.7
Dekker (DEN refined)	PW	29.5	32.9	95.7
Leitner et al. 2012	OMS	25.7	30.5	96.3
This Work (DEN refined)	OMS	24.8	28.3	95.5
Open Form (Bovine)				
Muñoz et al. 2011	-	-	-	74.0
This Work (DEN refined)	OMS	32.7	39.8	78.8

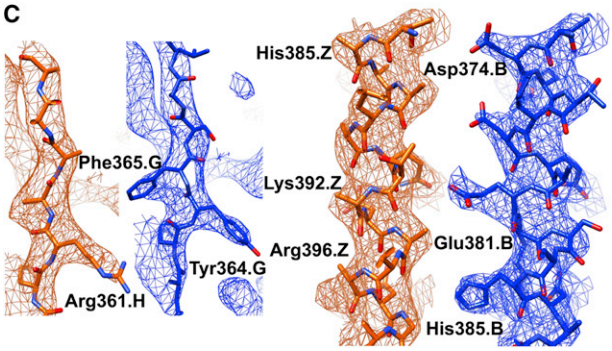

Figure 2. Refined X-Ray Structures
(A) An insertion (red) unique to the sequence of the CCT1-A subunit is well resolved as an additional density (delineated by arrows) in both the closed and open data sets. Such density is not observed in the adjacent CCT4-D subunit. Overlaid for scale on the CCT traces (green) is the backbone from the archaeal 1Q3R chaperonin template (black). Density is contoured at 2σ and 1σ for the closed and open forms, respectively. See also Figure S2.
(B) Refinement summaries for this work and for previous models of the same data sets. The PW subunit arrangement of the particle is that of Dekker et al. (2011), while the OMS arrangement (Kalisman et al., 2012) is as determined here.
(C) Snapshots at identical positions in the unit cell show that our model (blue) fits the $m2F_o$-DF_c electron density map better than the model of Dekker et al. (2011) (orange). The quality of the density is also improved, showing side-chains more clearly. Maps for both models are averaged over the four rings in the asymmetric unit and contoured at 2σ. Phases are calculated from the published coordinates.

and strongest interface (3-G/6-Z) are flanking 6-Z/8-Q on both sides. We note, however, that their deviations from the average values are not nearly as drastic as that of 6-Z/8-Q and thus might not have functional relevance.

Between their apical domains, the 6-Z and 8-Q subunits are pushed apart because of the strain exerted by the strong kink in the helix of the 6-Z subunit that caps the folding chamber (Figure 3B). An analysis of the evolutionary conservation at the interface (Figure S3) implicates residue Arg259 at the tip of that helix as a probable cause of the kink. This arginine is fully conserved in the CCT6-Z subunits of all eukaryotes, but its paralogous positions in the other seven subunits are always hydrophobic and

Table 2. Contact Areas at the Subunit Interfaces within a Ring

		Subunit Pair (Sum of Voronoi Face Area; Å^2)							
Left	Right	AG	GZ	ZQ	QH	HE	EB	BD	DA
equatorial	equatorial	844	899	**460**	770	572	717	761	710
middle	equatorial	642	642	369	504	**358**	571	608	392
apical	apical	1,065	1,252	**796**	911	1,242	1,139	1,192	985
other		303	283	**47**	220	620	271	189	472
total		2,854	3,076	**1,627**	2,405	2,792	2,698	2,750	2,559

Surface area values are calculated from a Voronoi decomposition using the program by Gerstein and Chothia (1996). Left and right domains refer to the subunits as written in the letter pairs. The residue ranges of the domains are listed in Table S1. Low values are bold and high values are underlined.

part of the hydrophobic core of the cap. The burial of the arginine side-chain in the hydrophobic core displaces the tip of the 6-Z capping helix in a direction consistent with the kink. In contrast to that example, at other positions along the 6-Z/8-Q interface, the structural weakness is coupled to loss of evolutionary conservation. For example, between the equatorial domains, we find Leu43 in CCT6-Z and Ser540 in CCT8-Q, which are not conserved. Yet the paralogous positions at the other seven interfaces are highly conserved. Overall, these data strongly suggest that the weak 6-Z/8-Q interface is not a crystallographic artifact but an intrinsic property of the closed form with functional importance. The most plausible functional explanation is that the mechanical opening of the ring starts at this interface during the transition to the open form.

The Chain Termini

The subunits of CCT have long N and C termini that are in most cases 10–20 residues long. All termini protrude from the lower part of the equatorial domains into the inner side of the particle, where they were long conjectured to form a flexible "septum" that separates the inner cavities of the two rings. We observed strong residual electron density at the midsection of the closed form that certainly supports the existence of a septum. A structural analysis of the termini in the closed form yielded similar conclusions to those reported by Dekker et al. (2011). We find that the C termini are disordered, but the N termini could be traced for an additional five to ten residues outside the equatorial domain (about half their total lengths). The N termini of all the subunits are traced inside the particle, with the exception of CCT4-D, whose N terminus is instead traced to the outside of the particle through an opening between the rings. The N termini inside the particle mainly interact with the previous subunit in the ring and in some cases with the abutting subunit on the other ring. We could not observe any common structural motif in the interactions of the N termini with the other subunits.

In sequence, the N and C termini are very different. The C termini are conserved across species both in their lengths and residue compositions, which are highly flexible and charged. The N termini, on the other hand, are much less conserved and contain more hydrophobic residues. The lax conservation and the lack of a common structural motif lead us to believe that the structured parts of the N termini do not carry a significant general function. Yet, a consequence of the unspecific "stickiness" of the N termini toward the inside surface of the particle is that they are not a significant part of the septum between the rings. It also means that it is mainly the C termini that interact with the substrate while it is in the folding chamber. Supporting evidence for this comes from a recent cross-linking study by Herzog et al. (2012), in which the C termini cross-linked to a substrate protein (2ABG) at about twice the rate of the

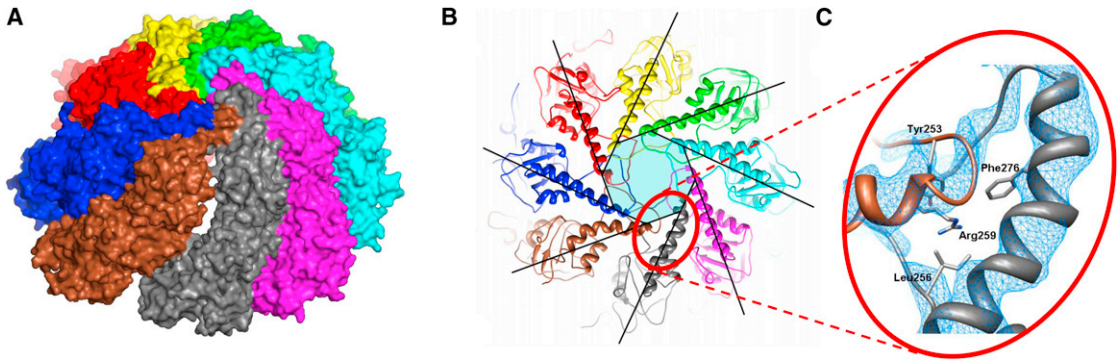

Figure 3. The Weak CCT6-Z/CCT8-Q Interface in the Closed Form

(A) A "crack" that occurs between these two subunits is not observed elsewhere. Only the top ring is shown. CCT6 is brown; CCT8 is gray.

(B) Top view of the closed form overlaid with a perfect 8-fold iris shows deformation of the Z capping helix. The region around Arg259 of CCT6-Z is marked.

(C) Arg259 is buried in the hydrophobic core of the cap with the guanidinium end group of the side chain exposed on the inner side of the particle. This exerts strain on the Arg259 position that is consistent with the helical deformation. In CCT6, this position is completely conserved across all eukaryotes. The corresponding positions in other subunits are always hydrophobic. The electron density map is averaged over the four rings in the asymmetric unit and contoured at 3σ. See also Figure S3.

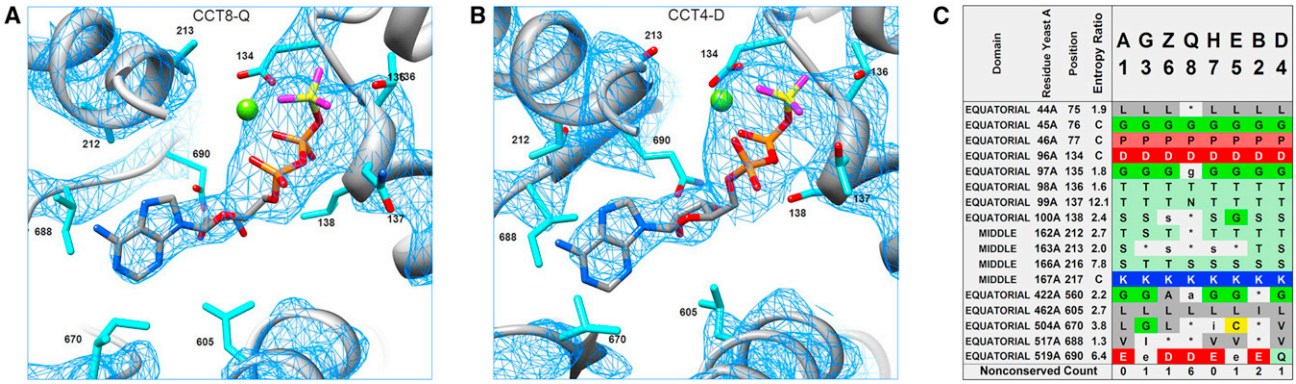

Figure 4. The ATP Binding Sites in the Closed Form

(A and B) The ATP sites of the CCT8-Q and CCT4-D subunits show the ADP-beryllium fluoride analogs (Be, yellow; F, magenta; Mg, green). The density corresponding to the adenosine and ribose moieties is well resolved in all subunits. Side-chains are labeled according to the position indices in the conservation analysis. The density is averaged over the four rings and contoured at 3σ.

(C) The evolutionary conservation of paralogous positions lining the ATP pockets in the eight subunits. The CCT8-Q subunit shows the most variation around the ATP site compared to the other seven subunits. Positions that are identical for at least 10 of the 13 tested eukaryotic species are marked by a capital letter. Positions that are identical for at least 7 of the 13 species are marked by a lowercase letter, and less conserved positions are marked by a star. High entropy ratio (see Experimental Procedures) marks signature positions that are highly conserved across species but differ between subunit types.

N termini. These functions of the C termini are also consistent with their evolutionary conservation.

ATP Binding and Hydrolysis

Every subunit contains a putative ATP-binding site. In the closed form, the ATP sites of all the 16 subunits contained strong densities that fitted well to a model of ADP, BeF_3, and Mg^{2+}, which was the nucleotide analog used to maintain the closed form. Specifically, the electron density corresponding to the adenosine and ribose moieties was well resolved in all the subunits (Figures 4A and 4B). We also did not observe any significant difference in the ADP binding modes between the subunits as far as permitted by the resolution. An analysis of the evolutionary conservation of residues lining the ATP pockets (Figure 4C) shows that they are highly conserved both across the thirteen tested species and across seven of the subunits. The exception is the CCT8-Q subunit that shows the largest variation from this consensus. For example, the GDGTT motif (positions 133–137) that occurs in all other subunits is mutated to GDGTN in CCT8-Q. Yet the mutations that distinguish the ATP site of CCT8-Q from other subunits are quite conserved across species. This indicates that, although the ATP site of CCT8-Q is modulated compared to other subunits, it still retains some ATP-related function. Our structure shows that part of this function is the binding (but perhaps not the hydrolysis) of ATP.

Finding ATP analogs in every subunit is also surprising given previous studies (Amit et al., 2010; Jiang et al., 2011; Reissmann et al., 2012), which showed that roughly just half of the subunits are actively hydrolyzing ATP. Therefore, while the closed structure implies that all subunits are fully capable of ATP binding, we do not think it reports on ATP hydrolysis. For hydrolysis, we turn to a study by Amit et al. (2010), which used the phenotypic effects of identical mutations in the ATP sites of the different subunits as a proxy to their ATP hydrolysis potencies. When we quantify these effects (see Experimental Procedures) and map them onto the ring order (Figure 5A), we find that they cluster: the ring section comprising of subunits CCT3-G, CCT6-Z, and CCT8-Q shows very little ATP hydrolysis. Very similar conclusions were also reached by a recent study (Reissmann et al., 2012) that used additional sets of mutations. In fact, the only serious discrepancy involves the classification of CCT7-H, which Reissmann et al. (2012) tagged as a weak ATP hydrolyzer. Since this subunit is between a subunit that clearly hydrolyzes ATP (CCT5-E) and a subunit that clearly hydrolyzes very little ATP (CCT8-Q), such discrepancy may arise from the different experimental setup. However, in our opinion, the strong sequence similarity of CCT7-H to the ATP-hydrolyzing subunits (see below) and the data of Amit et al. (2010) strongly suggest that CCT7-H is a potent ATP hydrolyzer.

Perhaps more problematic is the classification of CCT3-G, which according to our results is "halfway" in term of ATP-hydrolysis potency. The sequence similarity to other subunits is also ambiguous in its ability to classify this subunit. Interestingly, this duality is reflected in a recent study by Nadler-Holly et al. (2012) that linked CCT3-G to the binding of Q/N-rich protein substrates, a function we attribute more to the nonhydrolyzing subunits (see below). Yet that study also shows how this function is affected by a mutation in the ATP binding site of CCT3-G, indicating that ATP hydrolysis occurs.

Substrate Binding and Functional Partitioning

The initial studies cocrystallized CCT with two of its main substrates: actin in the closed form (Dekker et al., 2011) and tubulin in the open form (Muñoz et al., 2011). These substrates were too disordered for any backbone tracing and were reported as residual electron densities inside the rings. Our structures now enable us to locate the specific subunits that interact with these densities (Figure 5). In the open form, the residual tubulin density observed by Muñoz et al. (2011) is next to subunits CCT6-Z and CCT8-Q. In the closed form, we observed strong residual density inside the folding chamber next to subunits CCT3-G and CCT6-Z, which colocalizes with the

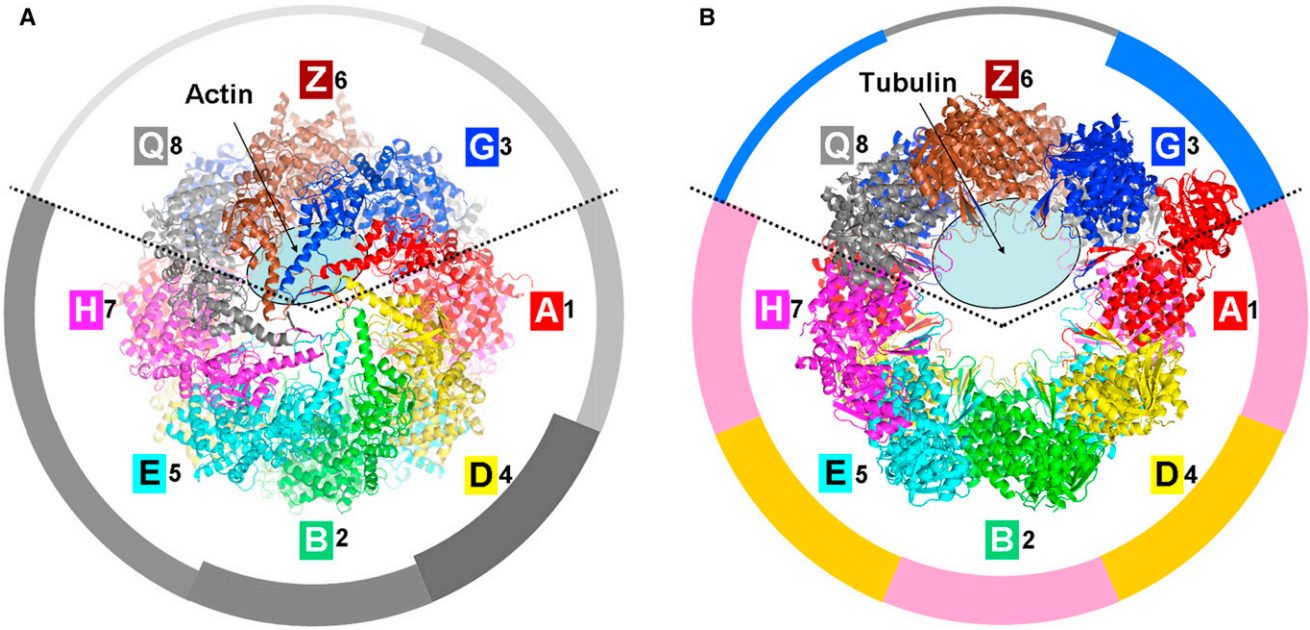

Figure 5. Substrate Binding and ATP Hydrolysis Are Partitioned in the CCT Particle

(A) Top view of the closed form with the location of residual actin density (Dekker et al., 2011) marked with an ellipse. The ATP hydrolysis potency of individual subunits (Amit et al., 2010; Experimental Procedures) is proportional to width in the surrounding pie chart.

(B) Top view of the open form with the location of residual tubulin density (Muñoz et al., 2011) marked with an ellipse. The average sequence identity of each subunit to all the others is proportional to width in the pie chart (see also Figure 6); groups of closest sequences are colored pink (A-1, B-2, and H-7) and ochre (D-4 and E-5). A ring partitioning emerges: subunits 3-G, 6-Z, and 8-Q are involved in substrate binding, while the other subunits are involved in ATP hydrolysis.

density observed by Dekker et al. (2011) in their initial study. Although the closed form was cocrystallized with Plp2 in addition to actin, we follow Dekker et al. (2011) in attributing this internal density to actin alone based on three arguments. First, Plp2 was shown by cryo-electron microscopy reconstruction to bind across and above the folding chamber (Martín-Benito et al., 2004), while this density is internal. Second, photo cross-linking located Plp2 close to CCT4-D (Dekker et al., 2011), which is far from the residual density. Finally, actin is much larger than Plp2. We did not observe any other substantial density that could locate Plp2.

Overall, the picture that emerges is that of a clearly partitioned particle. Subunits CCT3-G, 6-Z, and 8-Q bind the major substrates of CCT but have apparently lost their ATP-hydrolysis capabilities. They are located opposite in the ring to the five "power-subunits", those that strongly hydrolyze ATP: CCT7-H, 5-E, 2-B, 4-D, and 1-A. Of special interest is subunit CCT6-Z, which appears to play a central role in substrate handling. First, at the center of the substrate-binding section, it likely participates in the binding of both actin and tubulin. Second, it is involved in both the weakest and strongest intra-ring interfaces. Lastly, unlike its neighbor, CCT8-Q, its sequence is highly conserved across eukaryote species and shows sensitivity to mutations in putative substrate-binding residues (Lin et al., 1997). The central role of CCT6-Z may explain why this is the only subunit for which there is an expressed isoform in mammals. It is suggestive that such polymorphism achieves the highest flexibility in substrate handling for the minimal amount of gene duplication, since the ATP-utilizing section is unaltered.

Interestingly, the functional partitioning is mirrored in the mutual sequence similarity between subunits (Figures 5B and 6). The sequences of the five power-subunits are highly similar to each other, while the sequences of the substrate-binding subunits have diverged both from them and from each other. It is beyond the scope of this work to answer whether we are observing conservation pressure due to ATP-related functions or evolutionary diversification due to substrate-related functions (or both). Nonetheless, this partitioning adds new complexity to the intriguing issue of how this hetero-oligomeric complex evolved from its homo-oligomeric archaeal ancestor.

DISCUSSION

The unbiased approach presented here confidently assigns the correct subunit type to specific electron densities in crystallographic data sets of CCT. This allows us to link features in the structures to specific subunits, to match these features between structures, and to correlate other published data of CCT with the structures. The merging of these data on the two available structures of CCT shows that functions are clearly partitioned in the particle. We focus here on the implications of this partitioning on the opening of the particle. The particle opening is associated with the release of the ATP-hydrolysis products (Meyer et al., 2003). If indeed the particle first opens at the CCT6-Z/CCT8-Q interface as we suggest, and since very little of these products is occurring at these subunits, then the opening signal must propagate through nearly half the ring before achieving a mechanistic effect. While such a long route is in accord with

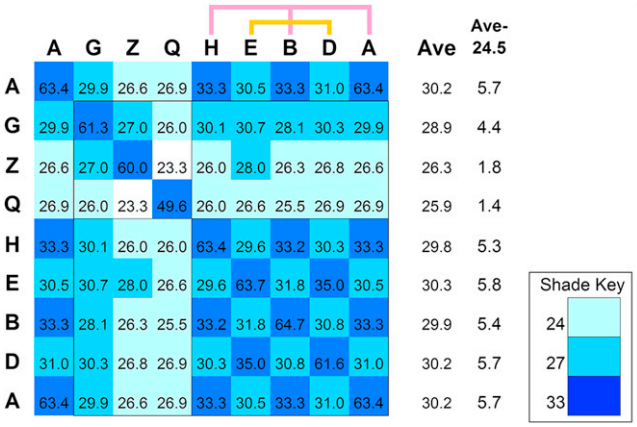

Figure 6. Sequence Identity among Subunit Types

The sequence identity between the CCT subunit types was calculated using a multiple sequence alignment of 13 species. The value shown for each subunit pair is the average percent identity of all the pairwise comparisons across species. The values are shaded to emphasize the closest subunit types, with 33% identity or more in dark blue, 27% or more in cyan, and 24% or more in light blue. The off-diagonal average values of each row are given in column "Ave" and indicate how close each subunit type is to all others. The modified value in column "Ave-24.5" is used to set the width of the pie chart segments in Figure 5B. Subunits that are close to one another can be arranged in two sets: (A), (B), and (H) and (D) and (E). Subunit CCT8-Q is significantly less conserved across species.

the sequential allosteric model assumed for CCT (Rivenzon-Segal et al., 2005), we cannot at present explain its benefit for CCT function. We would like to hypothesize that this mechanism somehow provides a longer lever in the conversion of the hydrolysis energy to mechanical pulling.

Our crystallographic methodology successfully demonstrates that useful side-chain information is available from data sets at resolutions as low as 5.5 Å. This surprising achievement requires that the direct observation of side-chain densities is replaced by an unbiased and automated approach. Since we worked with unprocessed data straight off the Protein Data Bank (PDB) site, we strongly believe that this approach would apply for any future crystallographic study of CCT. As such, our work paves the way for more routine structural studies of CCT, which will further enhance our understanding of this elaborate system. More broadly, we foresee it as a powerful tool for general low-resolution data where conventional crystallographic approaches cannot differentiate between similar models.

EXPERIMENTAL PROCEDURES

Crystallographic Data Sets

This study reanalyzes the crystallographic structure factors deposited by Dekker et al. (2011) under PDB codes 3P9D and 3P9E and by Muñoz et al. (2011) under PDB code 2XSM. Their publications fully detail the complex purification and crystallization steps, which we only briefly reiterate here. For the closed form, *Saccharomyces cerevisiae* CCT with the ANC2 mutation (G345D in CCT4; Shimon et al., 2008) was purified by using a 56-residues calcium-binding protein insert after residue P374 in CCT3 (Pappenberger et al., 2006). CCT was complexed with rabbit α-actin and Plp2 cofactor and induced into the closed conformation by incubation with ATP and beryllium fluoride. The complex was crystallized in a hanging drop in the presence of ATP and beryllium fluoride, and a 3.8 Å data set was collected (Table 1).

For the open form, CCT was purified from bovine testes and was verified by mass-spectrometry analysis to contain tubulin with the stoichiometry of one tubulin molecule per one CCT particle. CCT was incubated with ATP-γ-S, crystallized in hanging drop, and a 5.5 Å data set was collected (Table 1).

Homology Modeling of the Crystal Asymmetric Unit

Homology models of the individual yeast-CCT and bovine-CCT subunits were based on the template of the single repeating subunit from the archaeal thermosome of Thermococcus strain KS-1 (determined at 2.9 Å; PDB code 1Q3R) and on alignments adapted from our earlier work (Tables S2 and S3; Kalisman et al., 2012). We modeled all subunits with an identical backbone of 503 core residues by removing residues at alignment positions that had an insertion/deletion in any of the sequences. Side-chain positions were modeled by the SCWRL4 software (Krivov et al., 2009). To place a subunit model into the asymmetric unit, the model was broken into its three main domains (Table S1), and each domain was rigidly superimposed on the backbone coordinates deposited by the earlier studies (Dekker et al., 2011; Muñoz et al., 2011). The typical root mean square deviation was 0.6 Å per domain. The domain-wise model building increased the accuracy of our starting models by accounting for large variations in particle shape between thermosome and CCT. This model building protocol resulted in all-atom models for the asymmetric unit that had identical backbone coordinates, regardless of their subunit order, and only differed in the coordinates of the side-chain atoms.

Refinement of the Closed Form Model

Following the identification of the arrangement with the best crystallographic fit, we focused on its further refinement. The starting homology model had 4,024 (= 8 × 503) residues per ring, which constituted 92.0% of its total sequence lengths (not counting the calcium-binding protein insert). This model was initially refined with DEN (Brunger, 2007; Schröder et al., 2010) without imposed symmetry to R_{free} = 41.48%. For the next round of refinement, we introduced strong noncrystallographic symmetry (NCS) restraints designed to keep the structures of the four rings similar and used torsion-angle simulated annealing. We ran 24 parallel refinements that scanned the DEN parameter space by testing all combinations of the γ-parameter (0.0, 0.2, 0.4, 0.6, 0.8, and 1.0) and the DEN restraint weight (1.0, 10.0, 100.0, and 1,000.0). The largest drop in the R_{free} value to 36.9% was obtained for γ = 0.2 and wDEN = 1.0.

Subsequent refinement attempts were hindered by over-fitting, as indicated by the tendency of R_{free} to increase. We therefore switched to NCS constraints, which reduced the number of degrees of freedom 4-fold and allowed further refinement to R_{cryst}/R_{free} values of 27.06%/30.34%, respectively. Several model building and refinement cycles were performed, with all manual modeling done in COOT (Emsley et al., 2010). A total of 4,179 residues with all their constituent atoms were finally included in the ring model (95.5% of all residues). Rather than performing a costly DEN parameter search at each modeling/refinement cycle, we kept the γ value at 1.0 and the weight wDEN value at 100.0.

The density in the nucleotide-binding sites was not clear enough to unambiguously place the ADP molecule together with BeF_3 and the Mg^{2+} ion. The ADP•BeF_3•Mg complex was therefore restrained to maintain the coordination of BeF_3 and Mg with respect to the ADP molecule, as observed in the homologous site of the GroEL structure (PDB code 1SX3; determined at 2.0 Å).

A restrained ENCAD (Levitt et al., 1995) run was used to improve stereochemistry (Figure S4). Following the ENCAD run, we replaced some of the side-chain rotamers in the subunit interface regions (see Supplemental Information). These optimizations resulted in a drop of 0.3% in R_{free}.

In the last refinement round, the model quality was good enough to allow us to switch from torsion angle dynamics to Cartesian dynamics with DEN restraints. This further decreased R_{cryst}/R_{free} to 24.79%/28.37% to give our final structure. The effect of the DEN restraints is minimal at this stage of refinement: minimization of this final model in Cartesian coordinates without DEN restraints yields only slightly higher R_{cryst}/R_{free} values of 25.0%/28.5%, which indicates that the structure has been refined to a stable optimum.

Refinement of the Open Form Model

The models for the exhaustive R value analysis included only domains that were traced in the coordinates deposited by Muñoz et al. (2011). This meant that the subunits in the top ring comprised of all three domains (equatorial,

intermediate, and apical), but that the subunits in the bottom ring were mostly incomplete (only one subunit had all three domains, one subunit had two domains, and the other six subunits comprised only of the equatorial domain for a total of 1,142 missing residues compared to the top ring). Following the identification of the native arrangement of the asymmetric unit, we examined its electron density and found that the six missing intermediate domains in the bottom ring can all be docked into clear unassigned densities. Our starting model for refinement was therefore only missing seven apical domains in the bottom ring (total of 854 missing residues compared to the top ring). This model was refined by DEN using the default parameters. The resulting final structure had R_{cryst}/R_{free} of 34.0%/39.8%.

Quantification of the Phenotypes in Amit et al. (2010)

That study mutated a conserved aspartic residue at the ATP pocket of each subunit in turn and observed the resulting phenotypic effects on the yeast cells (mutation D96E in CCT1-A or its equivalents in the other seven genes). Despite the relatively benign nature of this mutation, the resulting phenotypic effects were drastic. Since this aspartic residue coordinates the magnesium ion at the ATP site, it is reasonable to assume that the severity of the phenotype is reporting on the extent of the ATP hydrolysis that occurs at each subunit. We quantified the severity of the phenotypes as described ahead and plotted these numbers for each subunit in Figure 5A. There were five quantifiable phenotypes measured by Amit et al. (2010): (1) growth rate at 15°C; (2) growth rate at 30°C; (3) growth rate at 37°C; (4) susceptibility to a toxic actin polymerization inhibitor, and (5) susceptibility to a toxic tubulin polymerization inhibitor. For each phenotype, we ranked the subunits according to the phenotype's severity going from one (least affected compared to wild-type) to eight (most affected). Since the mutation to CCT4 was lethal, CCT4 was always given the rank of eight. The "average phenotypic severity" of a subunit was then simply its average rank. The values calculated for subunits A, G, Z, Q, H, E, B, and D were 4.8, 2.8, 1.6, 1.6, 5.4, 5.4, 6.4, and 8.0, respectively.

Evolutionary Conservation and Sequence Identity between Subunits

CCT sequences for 13 species that span the eukaryote evolutionary tree were retrieved and aligned as previously described (Kalisman and Levitt, 2010). Entropy ratio is defined as

$$S_{RAT} = \frac{\sum_i n_i \ln(n_i)}{\sum_k \left(\sum_i m_{ki} \ln(m_{ki}) \right)}$$

where n_i and m_{ki} are counts of amino acid type i in all subunits or a specific subunit, k, respectively. Residues that are the same in all subunits are marked with "C" in the entropy ratio column.

ACCESSION NUMBERS

The coordinates and structure factors of the refined structures have been deposited in the Protein Data Bank under accession codes 4AOL and 4APK for particles 1 and 2 of the closed form, respectively, and 4B2T for the open form.

SUPPLEMENTAL INFORMATION

Supplemental Information includes four figures, three tables, and Supplemental Experimental Procedures and can be found with this article online at http://dx.doi.org/10.1016/j.str.2013.01.017.

ACKNOWLEDGMENTS

This work was supported by NIH grant GM063817. Computations were done on the Bio-X2 cluster (National Science Foundation award CNS-0619926). M.L. is the Robert W. and Vivian K. Cahill Professor of Cancer Research.

Received: December 5, 2012
Revised: January 20, 2013
Accepted: January 28, 2013
Published: March 7, 2013

REFERENCES

Amit, M., Weisberg, S.J., Nadler-Holly, M., McCormack, E.A., Feldmesser, E., Kaganovich, D., Willison, K.R., and Horovitz, A. (2010). Equivalent mutations in the eight subunits of the chaperonin CCT produce dramatically different cellular and gene expression phenotypes. J. Mol. Biol. *401*, 532–543.

Archibald, J.M., Blouin, C., and Doolittle, W.F. (2001). Gene duplication and the evolution of group II chaperonins: implications for structure and function. J. Struct. Biol. *135*, 157–169.

Brunger, A.T. (2007). Version 1.2 of the Crystallography and NMR system. Nat. Protoc. *2*, 2728–2733.

Cong, Y., Baker, M.L., Jakana, J., Woolford, D., Miller, E.J., Reissmann, S., Kumar, R.N., Redding-Johanson, A.M., Batth, T.S., Mukhopadhyay, A., et al. (2010). 4.0-A resolution cryo-EM structure of the mammalian chaperonin TRiC/CCT reveals its unique subunit arrangement. Proc. Natl. Acad. Sci. USA *107*, 4967–4972.

Dekker, C., Roe, S.M., McCormack, E.A., Beuron, F., Pearl, L.H., and Willison, K.R. (2011). The crystal structure of yeast CCT reveals intrinsic asymmetry of eukaryotic cytosolic chaperonins. EMBO J. *30*, 3078–3090.

Ditzel, L., Löwe, J., Stock, D., Stetter, K.O., Huber, H., Huber, R., and Steinbacher, S. (1998). Crystal structure of the thermosome, the archaeal chaperonin and homolog of CCT. Cell *93*, 125–138.

Emsley, P., Lohkamp, B., Scott, W.G., and Cowtan, K. (2010). Features and development of Coot. Acta Crystallogr. D Biol. Crystallogr. *66*, 486–501.

Gerstein, M., and Chothia, C. (1996). Packing at the protein-water interface. Proc. Natl. Acad. Sci. USA *93*, 10167–10172.

Herzog, F., Kahraman, A., Boehringer, D., Mak, R., Bracher, A., Walzthoeni, T., Leitner, A., Beck, M., Hartl, F.U., Ban, N., et al. (2012). Structural probing of a protein phosphatase 2A network by chemical cross-linking and mass spectrometry. Science *337*, 1348–1352.

Jiang, Y., Douglas, N.R., Conley, N.R., Miller, E.J., Frydman, J., and Moerner, W.E. (2011). Sensing cooperativity in ATP hydrolysis for single multisubunit enzymes in solution. Proc. Natl. Acad. Sci. USA *108*, 16962–16967.

Kalisman, N., and Levitt, M. (2010). Insights into the intra-ring subunit order of tric/cct: a structural and evolutionary analysis. Pac. Symp. Biocomput. *15*, 252–259.

Kalisman, N., Adams, C.M., and Levitt, M. (2012). Subunit order of eukaryotic TRiC/CCT chaperonin by cross-linking, mass spectrometry, and combinatorial homology modeling. Proc. Natl. Acad. Sci. USA *109*, 2884–2889.

Kapatai, G., Large, A., Benesch, J.L., Robinson, C.V., Carrascosa, J.L., Valpuesta, J.M., Gowrinathan, P., and Lund, P.A. (2006). All three chaperonin genes in the archaeon Haloferax volcanii are individually dispensable. Mol. Microbiol. *61*, 1583–1597.

Krivov, G.G., Shapovalov, M.V., and Dunbrack, R.L., Jr. (2009). Improved prediction of protein side-chain conformations with SCWRL4. Proteins *77*, 778–795.

Leitner, A., Joachimiak, L.A., Bracher, A., Mönkemeyer, L., Walzthoeni, T., Chen, B., Pechmann, S., Holmes, S., Cong, Y., Ma, B., et al. (2012). The molecular architecture of the eukaryotic chaperonin TRiC/CCT. Structure *20*, 814–825.

Levitt, M., Hirshberg, M., Sharon, R., and Daggett, V. (1995). Potential energy function and parameters for simulations of the molecular dynamics of proteins and nucleic acids in solution. Comput. Phys. Commun. *91*, 215–231.

Lin, P., Cardillo, T.S., Richard, L.M., Segel, G.B., and Sherman, F. (1997). Analysis of mutationally altered forms of the Cct6 subunit of the chaperonin from Saccharomyces cerevisiae. Genetics *147*, 1609–1633.

Llorca, O., Martín-Benito, J., Gómez-Puertas, P., Ritco-Vonsovici, M., Willison, K.R., Carrascosa, J.L., and Valpuesta, J.M. (2001). Analysis of the interaction between the eukaryotic chaperonin CCT and its substrates actin and tubulin. J. Struct. Biol. *135*, 205–218.

Martín-Benito, J., Bertrand, S., Hu, T., Ludtke, P.J., McLaughlin, J.N., Willardson, B.M., Carrascosa, J.L., and Valpuesta, J.M. (2004). Structure of the complex between the cytosolic chaperonin CCT and phosducin-like protein. Proc. Natl. Acad. Sci. USA *101*, 17410–17415.

Martín-Benito, J., Grantham, J., Boskovic, J., Brackley, K.I., Carrascosa, J.L., Willison, K.R., and Valpuesta, J.M. (2007). The inter-ring arrangement of the cytosolic chaperonin CCT. EMBO Rep. *8*, 252–257.

Meyer, A.S., Gillespie, J.R., Walther, D., Millet, I.S., Doniach, S., and Frydman, J. (2003). Closing the folding chamber of the eukaryotic chaperonin requires the transition state of ATP hydrolysis. Cell *113*, 369–381.

Muñoz, I.G., Yébenes, H., Zhou, M., Mesa, P., Serna, M., Park, A.Y., Bragado-Nilsson, E., Beloso, A., de Cárcer, G., Malumbres, M., et al. (2011). Crystal structure of the open conformation of the mammalian chaperonin CCT in complex with tubulin. Nat. Struct. Mol. Biol. *18*, 14–19.

Nadler-Holly, M., Breker, M., Gruber, R., Azia, A., Gymrek, M., Eisenstein, M., Willison, K.R., Schuldiner, M., and Horovitz, A. (2012). Interactions of subunit CCT3 in the yeast chaperonin CCT/TRiC with Q/N-rich proteins revealed by high-throughput microscopy analysis. Proc. Natl. Acad. Sci. USA *109*, 18833–18838.

Pappenberger, G., McCormack, E.A., and Willison, K.R. (2006). Quantitative actin folding reactions using yeast CCT purified via an internal tag in the CCT3/gamma subunit. J. Mol. Biol. *360*, 484–496.

Reissmann, S., Joachimiak, L.A., Chen, B., Meyer, A.S., Nguyen, A., and Frydman, J. (2012). A gradient of ATP affinities generates an asymmetric power stroke driving the chaperonin TRIC/CCT folding cycle. Cell Rep. *2*, 866–877.

Rivenzon-Segal, D., Wolf, S.G., Shimon, L., Willison, K.R., and Horovitz, A. (2005). Sequential ATP-induced allosteric transitions of the cytoplasmic chaperonin containing TCP-1 revealed by EM analysis. Nat. Struct. Mol. Biol. *12*, 233–237.

Schröder, G.F., Levitt, M., and Brunger, A.T. (2010). Super-resolution biomolecular crystallography with low-resolution data. Nature *464*, 1218–1222.

Shimon, L., Hynes, G.M., McCormack, E.A., Willison, K.R., and Horovitz, A. (2008). ATP-induced allostery in the eukaryotic chaperonin CCT is abolished by the mutation G345D in CCT4 that renders yeast temperature-sensitive for growth. J. Mol. Biol. *377*, 469–477.

Shomura, Y., Yoshida, T., Iizuka, R., Maruyama, T., Yohda, M., and Miki, K. (2004). Crystal structures of the group II chaperonin from Thermococcus strain KS-1: steric hindrance by the substituted amino acid, and inter-subunit rearrangement between two crystal forms. J. Mol. Biol. *335*, 1265–1278.

Spiess, C., Miller, E.J., McClellan, A.J., and Frydman, J. (2006). Identification of the TRiC/CCT substrate binding sites uncovers the function of subunit diversity in eukaryotic chaperonins. Mol. Cell *24*, 25–37.

Vaguine, A.A., Richelle, J., and Wodak, S.J. (1999). SFCHECK: a unified set of procedures for evaluating the quality of macromolecular structure-factor data and their agreement with the atomic model. Acta Crystallogr. D Biol. Crystallogr. *55*, 191–205.

Yébenes, H., Mesa, P., Muñoz, I.G., Montoya, G., and Valpuesta, J.M. (2011). Chaperonins: two rings for folding. Trends Biochem. Sci. *36*, 424–432.